Evaluation of Reduced Order Model for HT-9 Creep and Modifications to Current HT-9 Creep Model in BISON

September 30th, 2022

Technical Report

Ryan T. Sweet[1] and Stephen Novascone[1]

[1]Idaho National Laboratory

Idaho National Laboratory

Evaluation of Reduced Order Model for HT-9 Creep and Modifications to Current HT-9 Creep Model in BISON

Technical Report

Ryan T. Sweet[1] and Stephen Novascone[1]

[1]Idaho National Laboratory

September 30th, 2022

Page intentionally left blank

Abstract

In order to leverage existing reduced-order models (ROM) for material modeling, Los Alamos National Laboratory (LANL)-developed HT-9 cladding mechanistic-based constitutive models have been implemented into BISON. It is posited that the increased fidelity of the ROM will show improvement over engineering-scale models in terms of comparison against experimental measurements. Idaho National Laboratory will assist LANL in implementing an HT-9 ROM in BISON. Once the HT-9 mechanistic constitutive model can be leveraged in nuclear performance simulations, the numerical results of fast reactor models will be analyzed and compared against the Fuels Irradiation & Physics Database and separate effects tests to attempt a validation process. Idaho National Laboratory and LANL will work together to perform any necessary improvement identified during the implementation and use processes. Successful milestone completion will enable the general use of validated mechanistic ROMs for HT-9 cladding in BISON.

This report provides a brief introduction to the Los Alamos Reduced Order Model Applied to Nonlinear Constitutive Equations (LAROMance) code, mechanical testing used to illustrate its creep and plastic deformation predictions for HT-9 cladding, and a comparison with existing models implemented into BISON. Current models have been modified to more appropriately account for primary thermal creep, and results for corresponding testing are included in this report.

Page intentionally left blank

Page intentionally left blank

Contents

List of Figures

List of Tables

Acknowledgments

1. Introduction

The martensitic alloy, HT-9, is a candidate cladding and duct material for advanced reactors with sodium-cooled, sodium-bonded metallic fuels. HT-9 is a 12Cr-1Mo-V steel chosen because of demonstrated experience withstanding the expected irradiation and chemical environment under reactor-relevant mechanical and thermal loading [1]. Specifically, this alloy shows good corrosion behavior in sodium coolant, good irradiation dimensional stability at high doses owing to its BCC crystal structure, and it has been previously used as fuel cladding for irradiation experiments and driver fuel in the Experimental Breeder Reactor II (EBR-II) [2, 3].

During the fuel irradiation, the cladding tube is expected to deform due to the evolving pressure differential between the cladding tube interior and coolant system pressure and due to the diametral expansion of the fuel as it swells from fission [4]. In order to calculate the cladding deformation accurately, the creep and plastic deformation of the cladding must be accounted for. As the fuel is utilized, the buildup of both solid and gaseous fission products causes to the fuel to swell, increasing the fuel diameter and eventually reaching the cladding tube interior. Although the cladding is more rigid than metallic fuels, fuel-cladding mechanical interaction will cause a tensile stress in the cladding, allowing it undergo a slight deformation to relieve the stress. As the fuel utilization continues, gaseous fission products are released from the fuel and accumulate in the rod plenum, increasing the fuel rod internal pressure. The pressure differential, which forms across the cladding tube, continues to increase with increasing fission gas release and continues to create a greater tensile stress loading across the cladding tube. Cladding thermal and irradiation creep are expected to play a significant role in the cladding alloy behavior and failure limit at these temperatures [~700–900 K] and neutron fluxes [~10^{19}–$10^{20} n/m^2/s$].

This report documents ongoing efforts to improve creep calculations for HT-9 cladding tubes under expected irradiation and loading conditions. As part of this work, an HT-9 specific mechanistic creep model developed at Los Alamos National Laboratory (LANL) [5] has been incorporated into the BISON fuel performance code and evaluated. Current models have also been modified to improve the implementation of primary thermal creep and have have been evaluated and tested. An overview of the models (Chapter 2), testing results (Chapter 3), and a comparison of cladding profilometry (Section 3.3) for a fuel pin that underwent irradiation in EBR-II is also included here.

2. Creep Models for HT-9 Cladding

In this work, available creep models for HT-9 are assessed to determine how they compare and provide insight into their trends with changing conditions. The mechanistic model, Los Alamos Reduced Order Model Applied to Nonlinear Constitutive Equations (LAROMance), is evaluated for default and fitted model parameters. Additionally the current BISON creep models are modified to calculate primary creep more accurately. This section provides an overview of the LAROMance and BISON HT-9 creep models.

2.1   Los Alamos Reduced Order Model Applied to Nonlinear Constitutive Equations

Because of the the limited data available to generate an engineering-scale creep model that covers the entire expected operational condition space for HT-9 cladding, alternative methods are currently investigated to determine how best to develop and simulate a consistent model which can fill gaps in existing data ranges. One method developed at LANL is the use of a multiscale reduced order model (ROM), which effectively uses microstructural modeling to generate a database that can be sampled to generate an engineering-scale creep model [6][7]. This method utilizes a crystal plasticity constitutive model to simulate poly-crystals under a variety of microstructural and environmental conditions[8]. The resulting database of predicted mechanical responses encompasses the expected operating range of interest for the alloy, in this case HT-9. This model accounts for variability in the microstructure through the use of dislocation densities and an environmental dose rate factor. The implementation of the LAROMance surrogate material model, which contains the appropriate methods for sampling the material database and evolving the LAROMance model history dependent variables, is contained in MOOSE under *LAROMANCEStressUpdateBase*. The HT-9 material database that parameterizes the LAROMance surrogate material model is currently implemented in BISON, under *HT9LaRomance*. The LAROMance models allow for detailed microstructural data to be incorporated into the engineering-scale simulations without high computational costs and allow for data gaps to be filled using physics-based methods in the absence of experimental data. The LAROMance HT-9 model is implemented into BISON as a database and, therefore, does not have an engineering-scale functional form that the empirical models discussed later in this report do.

2.2 Metallic Fuels Handbook and Ryu, Kim, and Yacout Creep Correlations

The total creep rate calculation for HT-9 cladding in BISON is a combination of the thermal creep rate and irradiation creep rate, as shown in Eq. (2.1).

$$\dot{\epsilon}_{total} = \dot{\epsilon}_{th.total} + \dot{\epsilon}_{irr.total} \tag{2.1}$$

where $\dot{\epsilon}_{total}$ is the total creep strain rate over a time domain (nominally a timestep of the fuel performance code), $\dot{\epsilon}_{th.total}$ is the sum of all contributions to the thermal creep strain rate, and $\dot{\epsilon}_{irr.total}$ is the sum of contributions to the irradiation creep strain rate. To calculate the thermal creep strain rate, two empirical models currently exist for HT-9 cladding in BISON: one from the Metallic Fuels Handbook (MFH) [9] and the other developed by Ryu et al. (RKY) [10]. Although they present different functional forms, the underlying mechanics of their implementation into BISON is similar. The MFH [9] irradiation creep model for HT-9, shown in Eq. (2.2), is the only HT-9 irradiation creep model implemented in BISON.

$$\dot{\epsilon}_{irr.total} = \left[A_1 + A_2 \exp\left(\frac{-Q}{RT} \right) \right] \cdot \sigma^{1.3} \cdot \phi \tag{2.2}$$

where $\dot{\epsilon}_{irr.total}$ is the total irradiation creep strain (1/s), A1 and A2 are creep constants, Q is a thermal activation energy (kcal/mol), σ is the effective stress (MPa), and ϕ is the fast neutron flux ($\#/m^2/s$). Values and units for the terms in Eq. (2.2) are provided in Table 2.1.

Table 2.1. Parameters for HT-9 MFH irradiation creep model. [9]

Constants	Value	Units
A_1	1.83E-04	$MPa^{-1.3}$- m^2
A_2	2.59E+14	$MPa^{-1.3}$- m^2
Q	73000	kcal-mol^{-1}
R	1.987	kcal-K^{-1}-mol^{-1}

2.2.1 Metallic Fuels Handbook Thermal Creep Model

The total thermal creep rate ($\dot{\epsilon}_{therm.total}$) calculated by the MFH model Eq. (2.3) is the sum of three distinct creep rate regimes: the primary creep rate ($\dot{\epsilon}_p$), which quickly diminishes after a material is loaded; the secondary creep rate ($\dot{\epsilon}_s$), which is constant with stress and temperature; and the tertiary creep rate ($\dot{\epsilon}_t$), which becomes significant as the cladding approaches creep failure.

$$\dot{\epsilon}_{therm.total} = \dot{\epsilon}_p + \dot{\epsilon}_s + \dot{\epsilon}_t \tag{2.3}$$

The primary creep rate, Eq. (2.4), is the most significant creep mechanism immediately following loading and decays exponentially as the primary creep rate approaches a saturation value. The secondary thermal creep rate ($\dot{\epsilon}_s$) for the MFH model Eq. (2.5) remains constant in time and only varies with stress and temperature. For significant periods of the reactor operation, this is the dominant cladding creep strain contribution, as the primary creep rate decays (~1% of its original value after ~800 hours). The tertiary creep strain rate ($\dot{\epsilon}_t$), for the MFH model Eq. (2.6), increases

exponentially with time and, for this work, is not considered.

$$\dot{\epsilon}_p = \left[C_1 \exp\left(\frac{-Q_1}{RT}\right)\sigma + C_2 \exp\left(\frac{-Q_2}{RT}\right)\sigma^4 + C_3 \exp\left(\frac{-Q_3}{RT}\right)\sigma^{.5} \right] \cdot C_4 \exp\left(-C_4 t\right) \tag{2.4}$$

$$\dot{\epsilon}_s = \left[C_5 \exp\left(\frac{-Q_4}{RT}\right)\sigma^2 + C_6 \exp\left(\frac{-Q_5}{RT}\right)\sigma^5 \right] \tag{2.5}$$

$$\dot{\epsilon}_t = \left[4 \cdot C_7 \exp\left(\frac{-Q_6}{RT}\right)\sigma^{10} \right] \cdot t^3 \tag{2.6}$$

where $\dot{\epsilon}_p$ is the primary creep rate (1/s), $\dot{\epsilon}_s$ is the secondary creep rate (1/s), $\dot{\epsilon}_t$ is the tertiary creep rate (1/s), C_x are creep constants, Q_x are thermal activation energies (kcal/mol), σ is the effective stress (MPa), and t is the time (s). Constants and activation energies for the creep rate contributions for the MFH model are included in Table 2.2.

Table 2.2. Parameters for HT-9 MFH thermal creep model [9].

Constants	Value	Units	Constants	Value	Units
C_1	13.4	MPa^{-1}	Q_1	15,027	kcal-mol^{-1}
C_2	8.43E-03	MPa^{-4}	Q_2	26,451	kcal-mol^{-1}
C_3	4.08E+18	$MPa^{-0.5}$	Q_3	89,167	kcal-mol^{-1}
C_4	1.60E-06	s^{-1}	Q_4	83,142	kcal-mol^{-1}
C_5	1.17E+09	MPa^{-2}-s^{-1}	Q_5	108,276	kcal-mol^{-1}
C_6	8.33E+09	MPa^{-5}-s^{-1}	Q_6	282,700	kcal-mol^{-1}
C_7	9.53E+21	MPa^{-10}-s^{-2}	R	1.987	kcal-K^{-1}-mol^{-1}

In this implementation, the primary creep rate is dependant on time, and as such, continually diminishes after the simulation time begins. Effectively, this limits the amount of primary creep strain that a cladding tube would experience from an increased load later in operation. This is a fairly significant model shortcoming because the cladding is expected to experience an increasing tensile loading as the fission gas is released from the fuel during operation. To improve the handling of dynamic loading conditions, a slight modification has been made to the time dependence in the primary creep model to allow it to model primary creep strain regardless of the loading or simulation time. Similarly, the tertiary creep contribution is unstable in time, quickly increasing even at low temperatures and stresses. No modifications have yet been made to include this tertiary term, and it is not included in this work.

In order to alter the MFH primary creep strain rate model, the analogous primary creep strain is used and substituted into the time-dependant term. The MFH [9] defines the total primary creep as:

$$\epsilon_p = \left[C_1 \exp\left(\frac{-Q_1}{RT}\right)\sigma + C_2 \exp\left(\frac{-Q_2}{RT}\right)\sigma^4 + C_3 \exp\left(\frac{-Q_3}{RT}\right)\sigma^{.5} \right] \cdot \left(1 - \exp\left(-C_4 t\right)\right) \tag{2.7}$$

By taking the limit of the primary creep strain as t approaches ∞, the saturated primary creep, or the maximum amount of primary creep, can be determined, as shown in Eq. (2.8).

$$\lim_{t \to \infty} \epsilon_p = \epsilon_{p,sat.} = \left[C_1 \exp\left(\frac{-Q_1}{RT}\right)\sigma + C_2 \exp\left(\frac{-Q_2}{RT}\right)\sigma^4 + C_3 \exp\left(\frac{-Q_3}{RT}\right)\sigma^{.5} \right] \tag{2.8}$$

The fraction of primary creep strain applied can be expressed as a fraction of the current primary creep strain and saturated primary creep strain:

$$\epsilon_{fract} = \frac{\epsilon_p}{\epsilon_{p,sat.}} = \left(1 - \exp\left(-C_4 t\right)\right) \tag{2.9}$$

Solving for t and substituting it into the primary creep strain rate yields:

$$\dot{\epsilon}_p = \left[C_1 \exp\left(\frac{-Q_1}{RT}\right)\sigma + C_2 \exp\left(\frac{-Q_2}{RT}\right)\sigma^4 + C_3 \exp\left(\frac{-Q_3}{RT}\right)\sigma^{.5}\right] \cdot C_4 \left(1 - \epsilon_{fract}\right) \tag{2.10}$$

This new expression, as shown in Eq. (2.10), allows the primary creep strain rate to be expressed as a fraction of the primary creep applied instead of time. This allows for the calculation of primary creep independent of when the load was applied. This primary creep rate calculation, Eq. (2.10), is implemented into BISON and used in the MFH model for this work.

2.2.2 Ryu, Kim, and Yacout Thermal Creep Model

Similarly, the RKY thermal creep model, as it is implemented into BISON, consists of multiple creep contributions. In this model, however, there is no tertiary creep rate expression, only a primary and secondary creep rate component are considered, as shown in Eq. (2.11) [10].

$$\dot{\epsilon}_{therm.total} = \dot{\epsilon}_p + \dot{\epsilon}_s \tag{2.11}$$

The RKY primary creep rate ($\dot{\epsilon}_p$), Eq. (2.12), is expressed as the sum of two exponential functions (one for temperature and one for stress) multiplied by a time-dependant term to allow the primary creep rate to decay after loading. The secondary creep rate for the RKY model,($\dot{\epsilon}_s$), Eq. (2.13), is independent of time and expressed as an exponential with temperature and a stress term. Secondary creep is the overwhelming creep strain contribution for long-term fuel cladding operation.

$$\dot{\epsilon}_p = \left[10^{(C_1 - C_2/T)} \cdot \sigma^{(C_3 + C_4/T)}\right] \cdot C_5 \exp\left(-C_5 t\right) \tag{2.12}$$

$$\dot{\epsilon}_s = 10^{(-C_6 - C_7/T)} \cdot \sigma^{1.5} \tag{2.13}$$

where $\dot{\epsilon}_p$ is the primary creep rate (1/s), $\dot{\epsilon}_s$ is the secondary creep rate (1/s), C_x are creep constants, σ is the effective stress (MPa), and t is the time (s). Constants for the creep rate contributions for the RKY model are included in Table 2.3.

Although the primary creep rate for the RKY model Eq. (2.12) takes a much different form than the MFH model Eq. (2.4), the time dependence is identical, and the solution for modifying the model is the same as well. The same process for substituting the primary creep strain fraction for time was used for the RKY model, resulting in a solution Eq. (2.14) that allows for the calculation of the primary creep rate for time-independent loading. Eq. (2.14) is the primary creep strain rate implemented into BISON for the RKY thermal creep model and for this work.

Table 2.3. Parameters for HT-9 RKY thermal creep model [10].

Constants	Value	Units
C_1	.52	MPa^{-1}
C_2	2647.31	MPa^{-4}
C_3	1.09	$\text{MPa}^{-0.5}$
C_4	31.48	s^{-1}
C_5	2.11E-06	$\text{MPa}^{-2}\text{-s}^{-1}$
C_6	5.58	$\text{MPa}^{-5}\text{-s}^{-1}$
C_7	5562.28	$\text{MPa}^{-10}\text{-s}^{-2}$

$$\dot{\epsilon}_p = \left[10^{(C_1 - C_2/T)} \cdot \sigma^{(C_3 + C_4/T)} \right] \cdot C_5 \left(1 - \epsilon_{fract} \right) \qquad (2.14)$$

3. Verification and Testing

In order to assess how the models compare, simulations of uniaxial tension tests were performed for the LAROMance and MFH creep models (Section 3.1). These tests include various conditions in order to make general trend comparisons. To more fully illustrate how the models predict creep rates and total creep strain, contours were generated by varying the stress and temperature of each model (Section 3.2). The simulations are sampled at various times to determine the creep rate corresponding to the primary and secondary creep rates. Lastly, simulations were performed using a current BISON assessment case with known cladding axial profilometry at the end of life to compare models in a dynamic loading condition (Section 3.3).

3.1 Los Alamos Reduced Order Model Applied to Nonlinear Constitutive Equations

Uniaxial creep tests for HT-9 were developed in BISON to calculate the material's creep response under a variety of conditions using the LAROMance HT-9 and MFH creep models. These consist of a single tension specimen under a simulated constant load for 350 days. This time was arbitrarily chosen to be sure the cladding tension sample had reached a strain where the primary creep had saturated and the creep was predominantly secondary creep. This allowed for single simulations where the primary creep rate could be sampled at the beginning of the simulations and the secondary creep rate and total strain at the end. The ROM was evaluated at varying temperature and stresses (Section 3.1.1), dose rates (Section 3.1.2), and initial cell and wall dislocation densities (Section 3.1.3). Additionally, a comparison was made with a previous separate effects analysis on HT-9 with BISON (Section 3.1.4)[11]. For these tests, a default initial cell dislocation density of 5.0e12 m^{-2} and an initial wall dislocation density of 6.0e12 m^{-2} are used unless otherwise specified.

3.1.1 Temperature and Stress

The first series of uniaxial creep tests conducted was targeted to assess the stress and temperature dependence of the creep models. For this series, the creep strain rate for the ROM and MFH model were assessed under constant loads of 10, 50, and 100 MPa at temperatures of 673 (Fig. 3.1), 773 (Fig. 3.2), and 873 K (Fig. 3.3). By changing the tension test loading, the general trend of the cladding strain rates between the models can be compared. In Fig. 3.1, the creep rate for the ROM is not as clearly delineated as it is for the MFH model; although, the logarithmic scale needed due to

the MFH model is quite large, which limits fine detail resolution. At such low temperatures for the alloy, low thermal creep rates are expected, even at higher stresses. For the MFH model, the primary creep rate saturation behavior can be seen until the secondary creep rate becomes dominant at ~125 days.
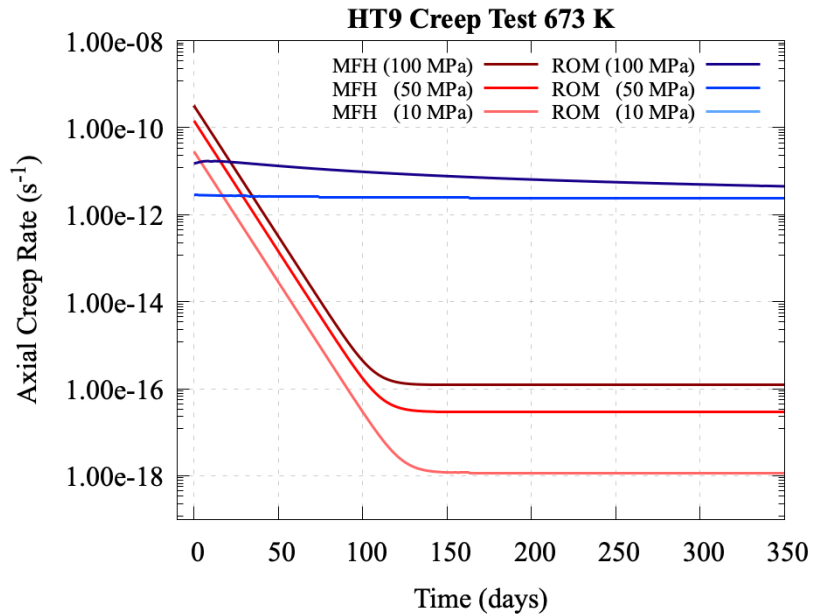

Figure 3.1. Creep strain rates at 10, 50, and 100 MPa for the MFH model and ROM at 673 K. Note: Creep strain rates for the 10 and 50 MPa tests using the ROM overlap.

At 773 K, as shown in Fig. 3.2, a much more clear delineation of the ROM creep rate curves with increasing stress is illustrated. In this figure, clear primary creep rate saturation can be seen within the first few days of the test. Although the 50 and 100 MPa curves briefly overlap, the creep rates are still low enough at these temperatures to likely play little role in the overall cladding overall deformation. Similarly, for the MFH model creep strain rate curves, as the temperature is increased, a clearer definition can be seen between curves. Notably, the ROM never reaches a flat steady-state creep rate. This plays a role in how the secondary creep rate is calculated later in this report.

As the temperature is increased further to 873 K, even more definition between the curves for the ROM is visible, as illustrated in Fig. 3.3. Interestingly, the 50 MPa creep rate curve resides above the 100 MPa curve for much of the tensile test, likely due to the interpolation between the areas of parameter space inherent in the construction of the surrogate model. As the temperatures are increased, the creep strains calculated by the MFH model at 50 and 100 MPa gradually increase past the ROM, which can be seen when comparing Fig. 3.1–Fig. 3.3.

Next, the creep rates from ROM were analysed using a 50 MPa load at temperatures starting at 673 K and increasing in 25 K increments to 898 K. Fig. 3.4 shows the creep strain rates over time for these tests. While the curves show generally expected behavior, there are a few details to identify within this figure. Firstly, at the higher temperatures, the primary creep rates become more pronounced. For the MFH model, these strain rate slopes do not vary because they correspond to the primary creep decay term, which is temperature and stress independent. Secondly, the curves are
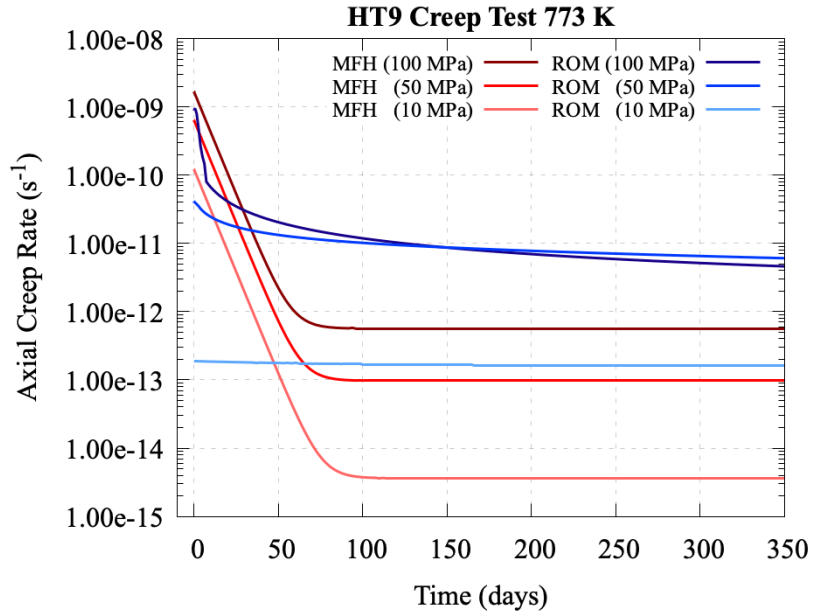
HT9 Creep Test 773 K

Figure 3.2. Creep strain rates at 10, 50, and 100 MPa for the MFH model and ROM at 773 K.
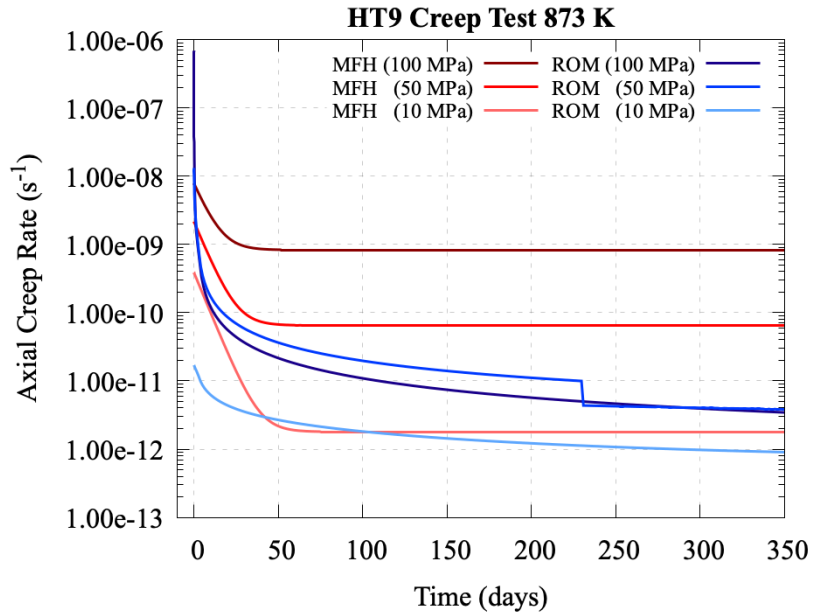
HT9 Creep Test 873 K

Figure 3.3. Creep strain rates at 10, 50, and 100 MPa for the MFH model and ROM at 873 K.

not monotonically increasing with increasing temperatures. For example, the 673 K creep rate overlaps and increases above the 723 K creep rates. Lastly, some discontinuities are illustrated due to the interpolation scheme, such as the jump in the 873 K curve at ~230 days.
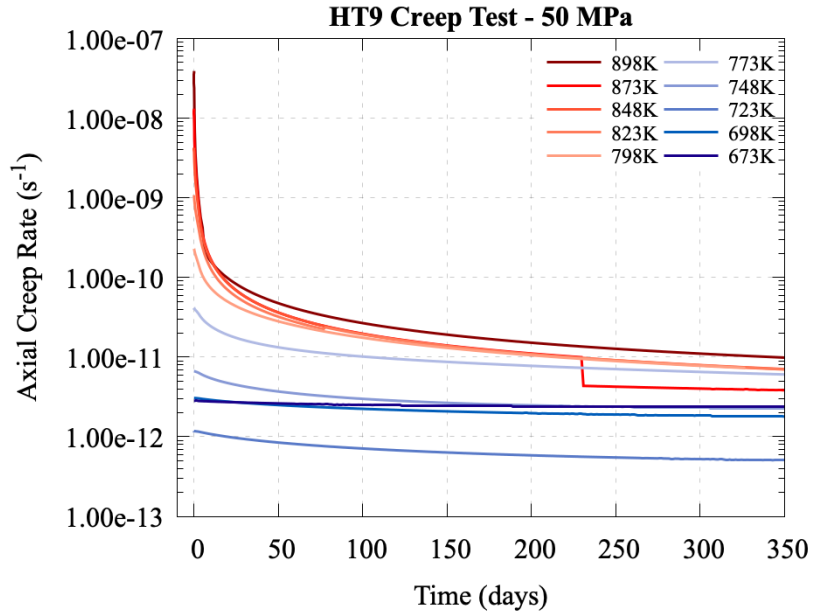
HT9 Creep Test - 50 MPa

Figure 3.4. Creep strain rates over time for the ROM under a 50-MPa axial stress at different testing temperatures.

3.1.2 Environmental Factor (Dose Rate)

For the ROM, an environmental factor is used that specifies the dose rate (in dpa/s) of the HT-9. To convert to a fast neutron flux, a value of 1 dpa/s $= 2.0e25$ $n/m^2/s$ is used. This allows the ROM and MFH to be compared correspondingly. Fig. 3.5 shows the creep strain rates for the ROM and MFH models under 50 MPa of constant loading at 623 K. Notably, for the various dose rates, the ROM oscillates between strain rates of 1e-10 and 1e-11. At higher neutron fluxes, the MFH model shows nearly two order of magnitude greater creep strain rates.

3.1.3 Cell and Wall Dislocation Density

The initial cell and wall dislocation densities were varied to determine the impact they have on the creep rates. For these tests, the densities were evaluated at the model default values and then an upper and lower value was chosen. The initial cell dislocation density, shown in Fig. 3.6, was evaluated for densities between 4e12 (m^{-2}) and 6e12 (m^{-2}). By increasing the density of the cell dislocation density, the creep strain rate increased. For the higher values of dislocation density, the secondary creep rate also increased.

The initial wall dislocation density (Fig. 3.7) was evaluated in a similar method by selecting a range around the default value, between 5.63e12 (m^{-2}) and 7e12 (m^{-2}). Again, the increased dislocation densities facilitate higher creep rates. For the highest dislocation density, the increase seems to compound an increased creep rate.
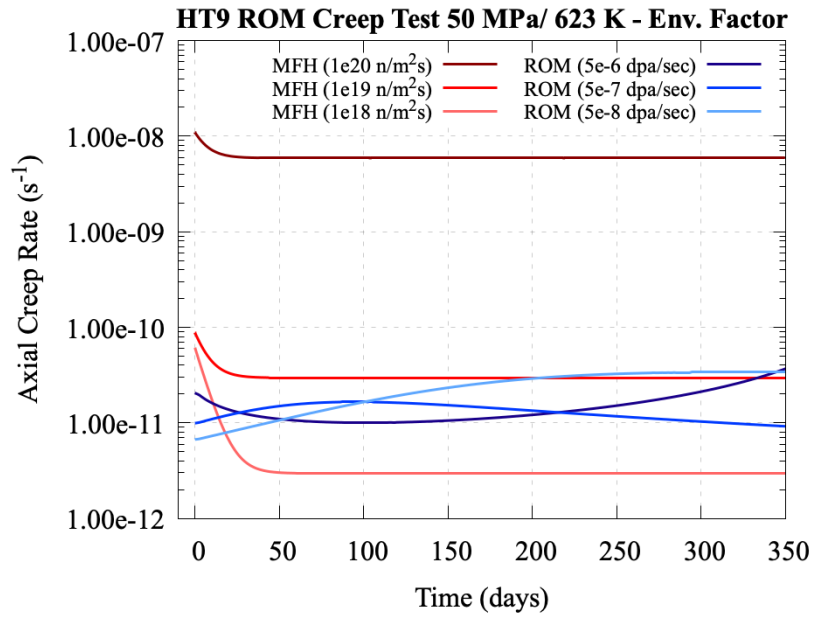
Figure 3.5. Creep strain rates over time for the ROM at different dose rates and the MFH model at corresponding fast neutron fluxes at 623 K and 50 MPa.
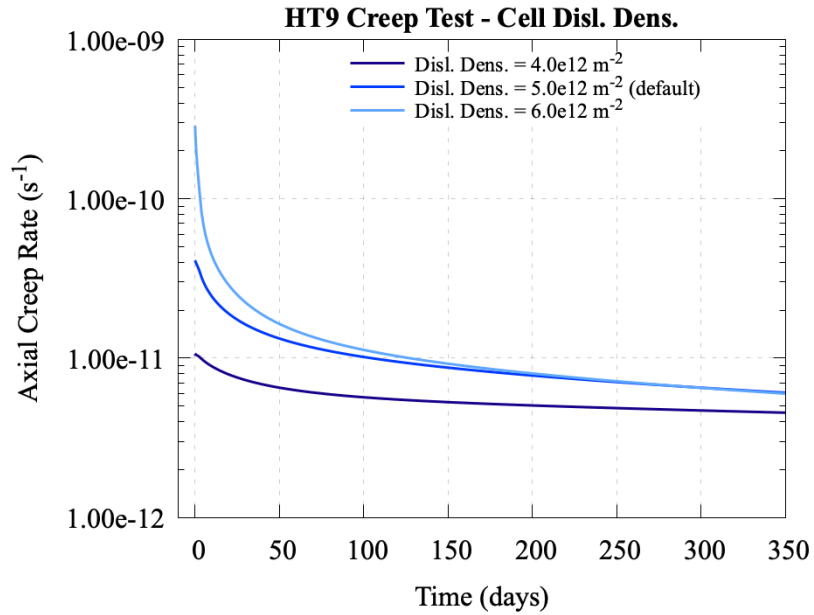

Figure 3.6. Creep strain rates over time for the ROM at different initial cell dislocation densities at 623 K and 50 MPa.
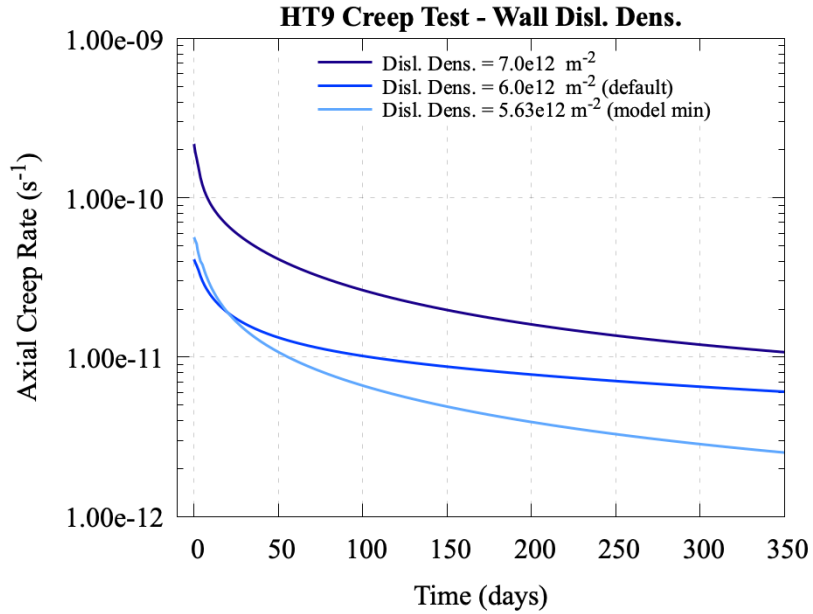
Figure 3.7. Creep strain rates over time for the ROM at different initial wall dislocation densities at 623 K and 50 MPa.

3.1.4 Separate Effects Testing

In this section, diametral strains from pressurized tube tests are used to compare against the creep models at different times during an irradiation [2]. In this case, a flux of 9.26e19 $n/m^2/s$ is assumed for these experiments. These simulations are similar to previous work on generating assessment cases for BISON [11]; however, they include a comparison with the ROM and a series of ROM simulations where the dislocation densities were modified to improve the diametral strain comparison. Experimental data for these simulations is derived from this former comparison [11]. For these simulations, the dislocation densities were the default values (initial cell: 5e12 m^{-2} and initial wall: 6e12 m^{-2}) for curves marked ROM and increased values were used for the curves marked ROM-Disl.Dens.Modified (initial cell: 6e12 m^{-2} and initial wall: 9e12 m^{-2}).

Fig. 3.8 shows a diametral strain comparison for a tube pressurized to reach a 110-MPa hoop stress at 425°C using the various creep models against the experimental measurement. The unmodified ROM shows a nearly straight diametral strain with an increasing neutron fluence, while the modified profile shows a much sharper increase in primary strain and a similar slope at higher neutron fluences. When changing the dislocation densities for this comparison, the profile of the curve did not change substantially; however, the magnitude of the creep strain did. The MFH model was added for a reference point and shows a ~25% overprediction in the creep strain calculation.

A similar process was used to compare against another pressurized tube experiment, this time at a 55-MPa hoop stress and 590°C, as shown in Fig. 3.9. Again, by using the modified dislocation densities, the ROM produces more comparable results than the unmodified ROM. Guidance is needed on the particular method to set the dislocation densities *a priori*, as they have a substantial impact on the cladding behavior. Additionally, because this is a physics-based model and not all cladding samples are microstructurally characterized, perhaps more general relations can be

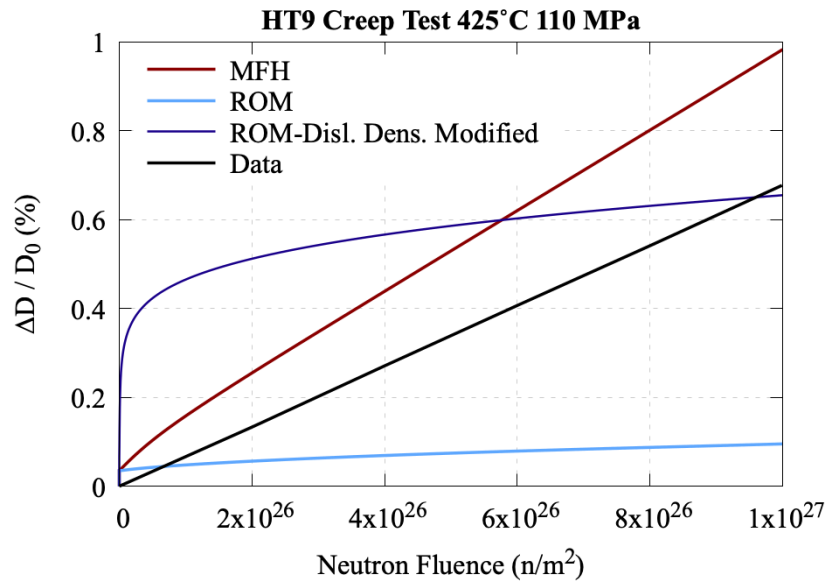used in place of the dislocation densities, such as grain size.

HT9 Creep Test 425˚C 110 MPa

Figure 3.8. Diametral strain as a function of neutron fluence for the HT-9 ROM, MFH model, and experimental data at 425°C and 110 MPa.
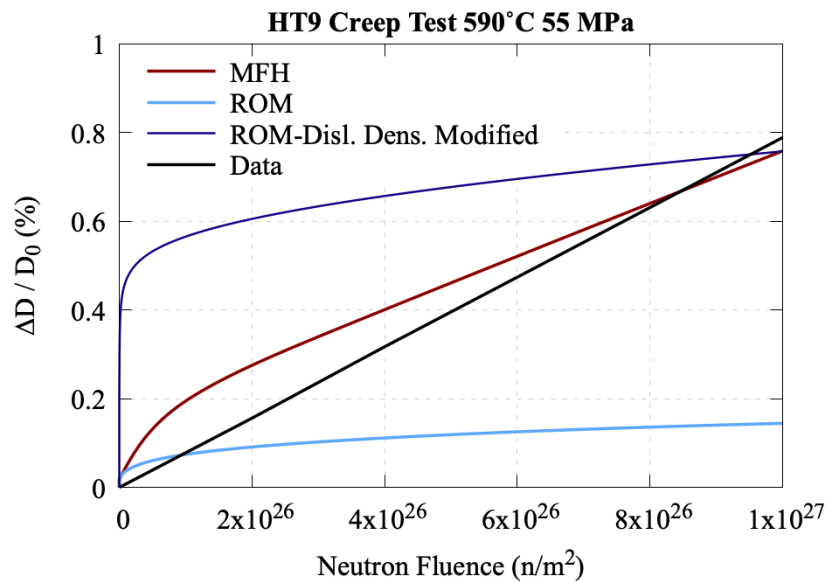
HT9 Creep Test 590˚C 55 MPa

Figure 3.9. Diametral strain as a function of neutron fluence for the HT-9 ROM, MFH model, and experimental data at 590°C and 55 MPa.

3.2 HT-9 Model Comparison

To generate a full illustration of the creep rate as a function of the temperature and stress, uniaxial creep tests were performed over the expected temperature [650–900 K] and stress [0–160 MPa] parameter space. Creep rates for the tension tests were sampled during the first full loading time step to determine the initial primary creep rate and again at 350 days, where the secondary creep rate is dominating the creep strain.

3.2.1 Primary Creep Rates

To evaluate the primary creep strain rate, ~10,000 uniaxial simulations were performed varying the temperature and stress within the expected operating parameters for HT-9 cladding. The creep strain rate was sampled at the beginning of the simulation, and the results were interpolated into exponential contours, as shown in Fig. 3.10. This figure shows an exponential increase in the primary creep strain for the MFH creep model, as expected from Eq. (2.10) where the current fraction of primary strain is zero. The "thinner" contours in the upper right demonstrate an acceleration in the creep rate at higher stresses and temperatures.

Conversely, for the RKY model (shown in Fig. 3.11), the contours show a deceleration in the creep rate with increasing stress and temperature (the contour width is increasing); although, the absolute creep rate for much of the center region of the contour is larger than the MFH model calculates.
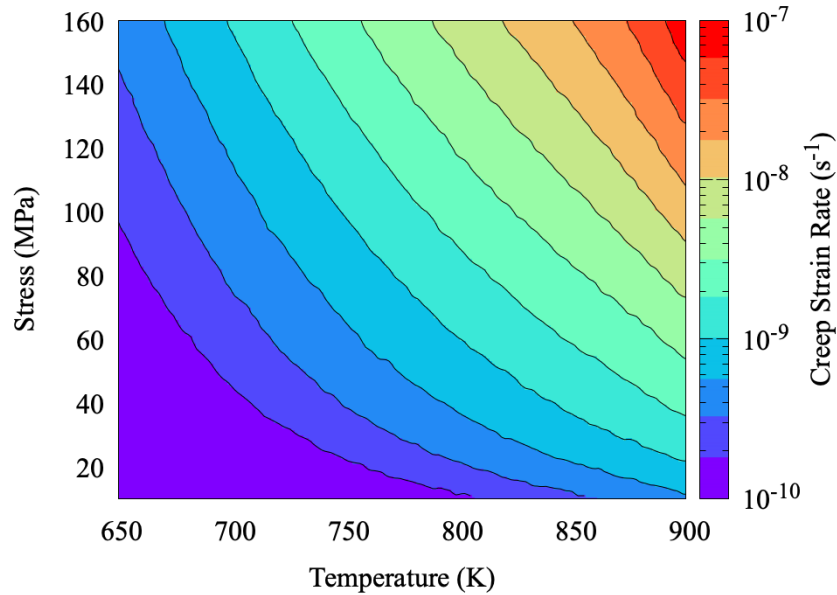

Figure 3.10. Primary creep strain rate for the MFH model as a function of temperature and stress.

The primary creep rate contour for the ROM is shown in Fig. 3.12. The creep rate trend for the ROM is a bit less intuitive than the MFH and RKY empirical models; although, it generally increases with stress and temperature. There are two exceptions here: one above 60 MPa and 800 K and the other at 40 MPa and 875 K. In this first region, the
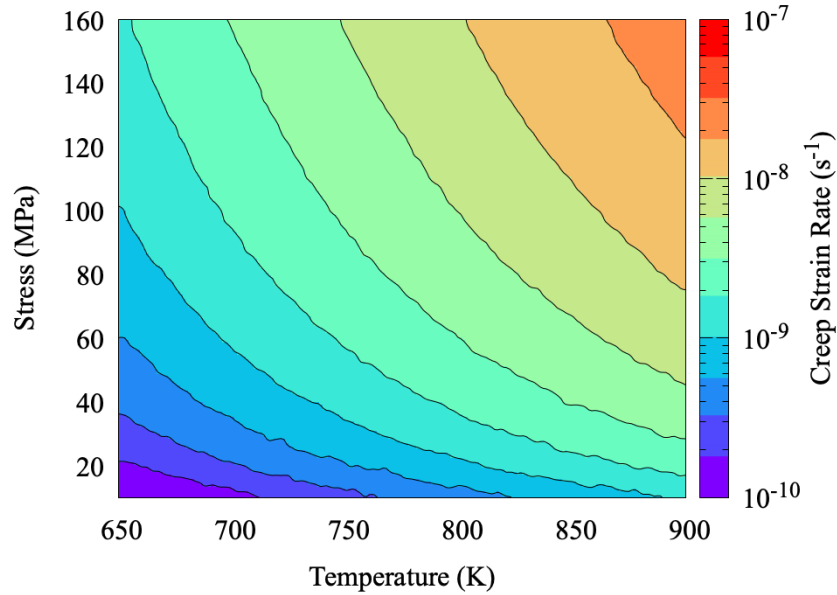
Figure 3.11. Primary creep strain rate for the RKY model as a function of temperature and stress.

creep rate has an inflection where the creep rate begins to decrease with increasing stress. The second region consists of an "island" with a higher creep rate and a sharp boundary. For these model, there are convergence issues in the simulations in these regions.

3.2.2 Secondary Creep Rates

To extract the secondary creep rates from the uniaxial simulations, the simulations were sampled at ~350 days. This sampling was performed to ensure that the primary creep rate had decayed and the secondary creep was dominating the creep rate of the HT-9. The MFH creep model (Fig. 3.13) shows a fairly rapid increase in the creep rate; although, it remains several orders of magnitude lower than the primary creep rate under equivalent conditions. This figure is truncated by the narrow range of creep rate contours used due to the ranges of the other models. Creep rates below 1e-11 s^{-1} are generally negligible on the timeframes considered for reactor fuel cladding (~5–10 years). The RKY creep model (Fig. 3.14) shows a more gradual increase in the creep rate and maintains a much greater creep rate than the MFH model through the entire stress and temperature region. Fig. 3.15 shows the secondary creep rate using the ROM over the same stress and temperature region. In this figure, areas of white space show simulation parameters where the uniaxial tension tests failed to solve. As compared to the empirical models the model trends are more sporadic, although the empirical model are generally simplified due to limited experimental conditions. Notably, there is a sharp region below 40 MPa and 700 K where the creep rate is reduced to a negligible value. Similarly to the primary creep rate calculation, the secondary creep contour shows similar regions where the creep rate decreases with increasing temperature and stress.
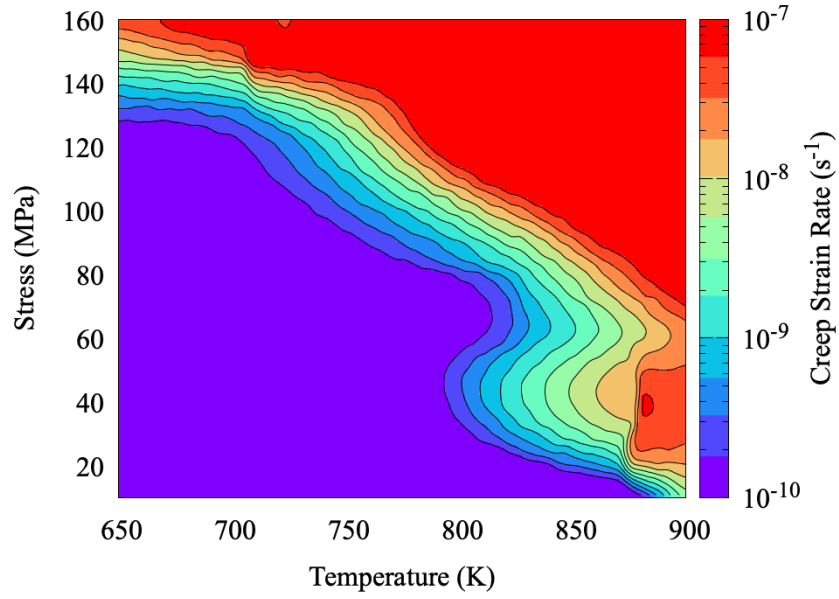
Figure 3.12. Primary creep strain rate for the ROM as a function of temperature and stress.
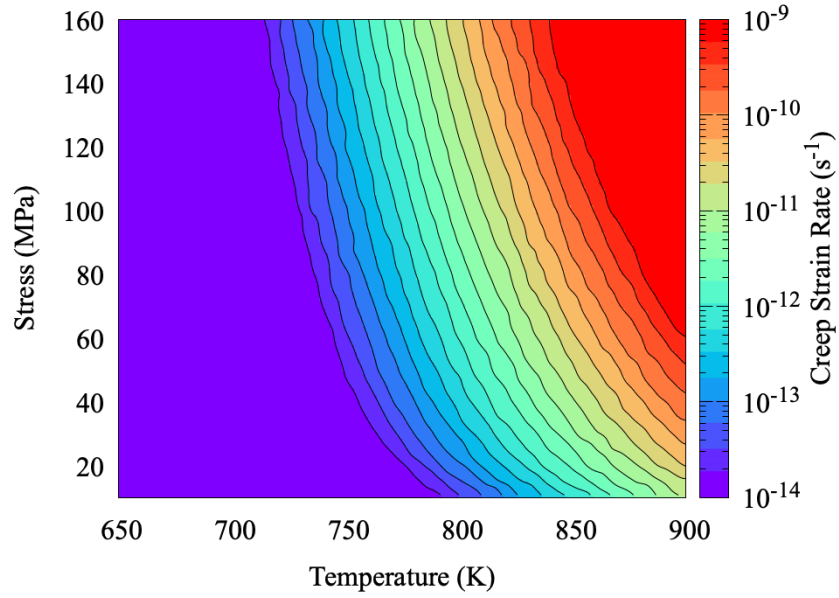

Figure 3.13. Secondary creep strain rate for the MFH model as a function of temperature and stress.
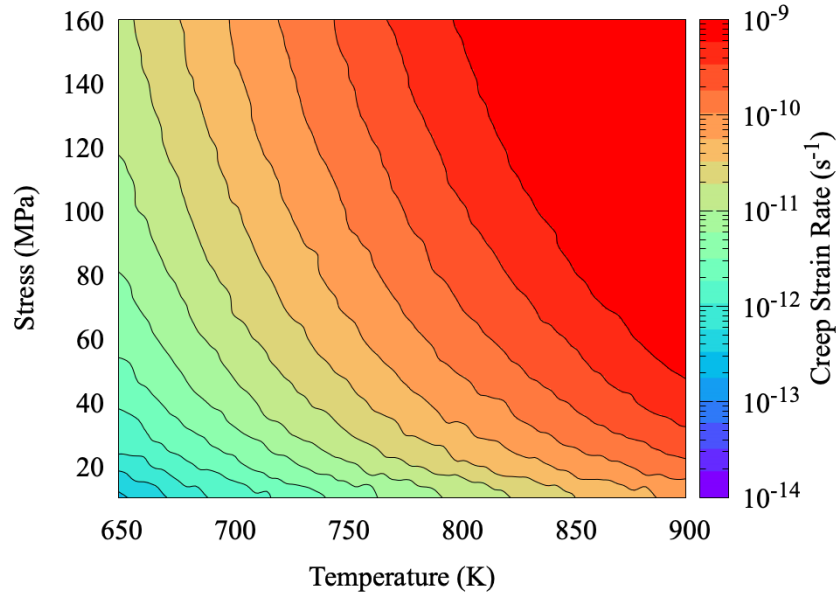
Figure 3.14. Secondary creep strain rate for the RKY model as a function of temperature and stress.
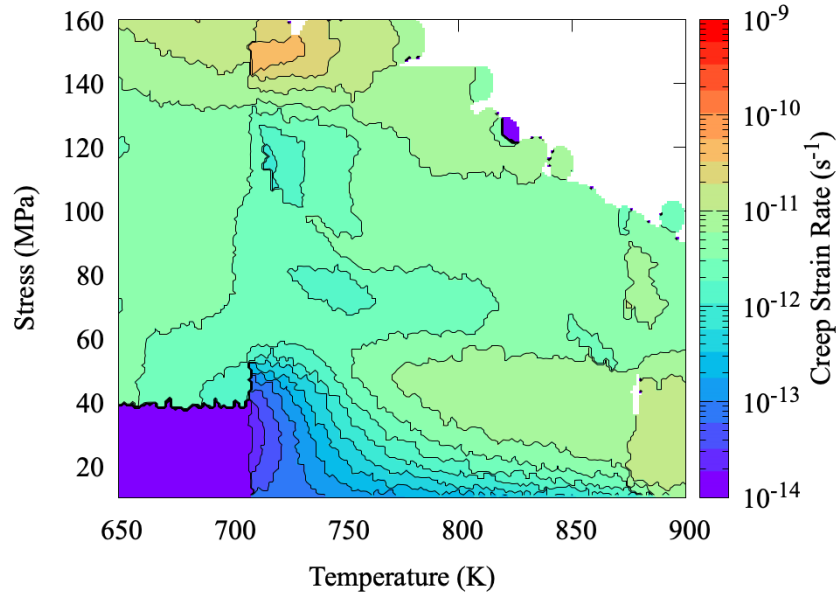

Figure 3.15. Secondary creep strain rate for the ROM as a function of temperature and stress.

3.2.3   Total Creep Strain

The total creep strain from the uniaxial tests is sampled at ~350 days. This sampling was performed to demonstrate how much more the secondary creep rate contributes to the overall creep strain than the primary creep rate over this

simulated time frame. As expected, the resulting total creep strain contours from the uniaxial tests show features of both the previous primary and secondary creep rate contours; however, because of the simulation timing, the secondary creep strain is much more significant.

The total creep strain for the MFH model is shown in Fig. 3.16. As with the primary and secondary creep strain rate, the creep rate not only increases, but accelerates, as it approaches high stresses and temperatures. This trend is not seen in the RKY model (Fig. 3.17), which maintains a steady increase in the creep strain with increasing temperature and stress. The ROM creep strain (Fig. 3.18), as expected, shows features of the primary and secondary creep rates. In magnitude, the ROM is similar to the MFH model at intermediate stresses [~60–120 MPa] and temperatures [~700–850 K].
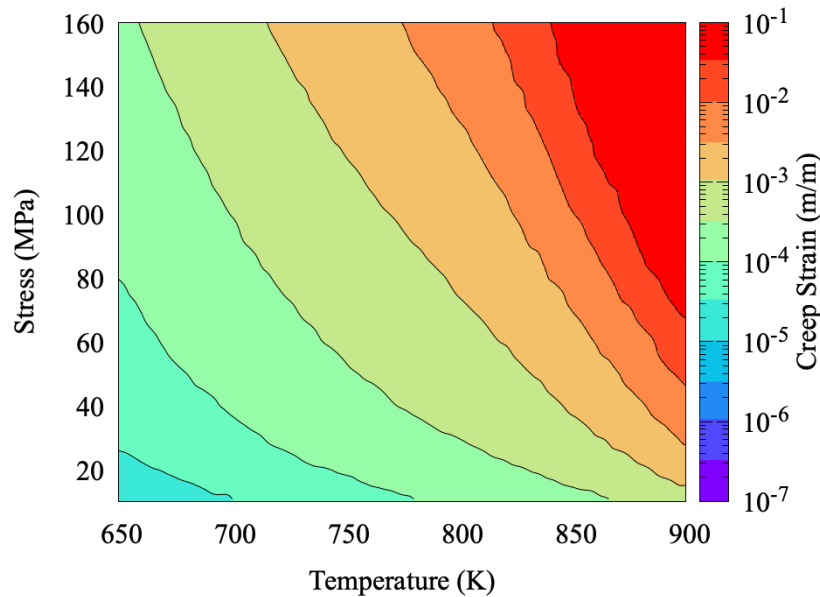

Figure 3.16. Creep strain for the MFH model at 350 days as a function of temperature and stress.

3.3 Cladding Profilometry Results

Up to this point, only uniaxial simulations have been considered, where the load is applied immediately effectively circumventing the modifications to the primary creep rate calculation. In order to evaluate how these changes modify the expected cladding strain profiles, an EBR-II fuel rod from the X441 sub-assembly was simulated for both the MFH and RKY creep models using the original and modified primary creep rate implementation. Simulations using the ROM had convergence issues and are not included in this work.

Cladding radial deformation profiles were generated at the end of life for the selected rod to identify the cladding deformation difference from the primary creep modification. Fig. 3.19 shows the cladding radial deformation along the fuel rod height for the modified and original creep implementations. In this example, the updated primary calculation
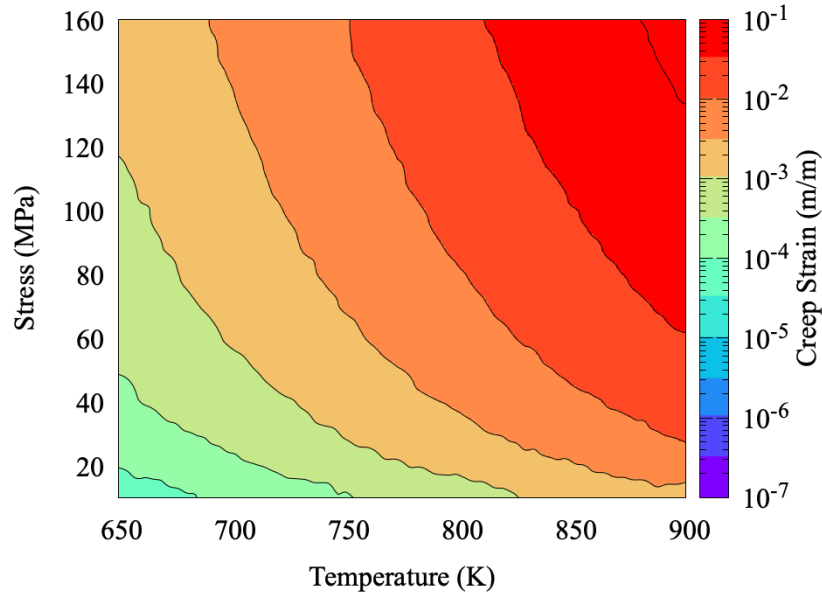
Figure 3.17. Creep strain for the RKY model at 350 days as a function of temperature and stress.
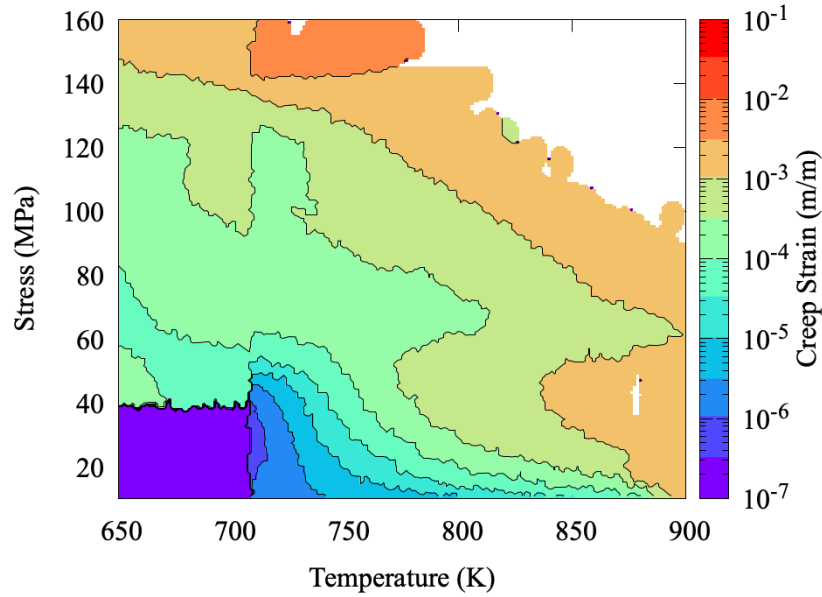

Figure 3.18. Creep strain for the ROM at 350 days as a function of temperature and stress.

shows a consistent increase in the cladding radial deformation, reaching approximately ~1 µm or ~15% of the overall cladding deformation.

The radial cladding deformation for the RKY model (Fig. 3.20) is substantially increased as compared to the MFH

model. For similar stresses and temperatures (80 MPa and 750 K),Fig. 3.16 and Fig. 3.17 show about a order of magnitude in the difference of the calculated creep strains. This shows in increase over the original model of nearly 10×. This is not entirely unexpected, as the cladding strain increases, so does the stress increase as the cladding thins. Poisson's effect can enhance the cladding deformation rate like it is in this scenario. A comparison with cladding profilometry would help this analysis and provide a point of reference for whether the cladding profiles are being calculated accurately.

Figure 3.19. Difference in radial displacement along the cladding for a fuel pin from the X441 sub-assembly using the modified and original MFH creep model.
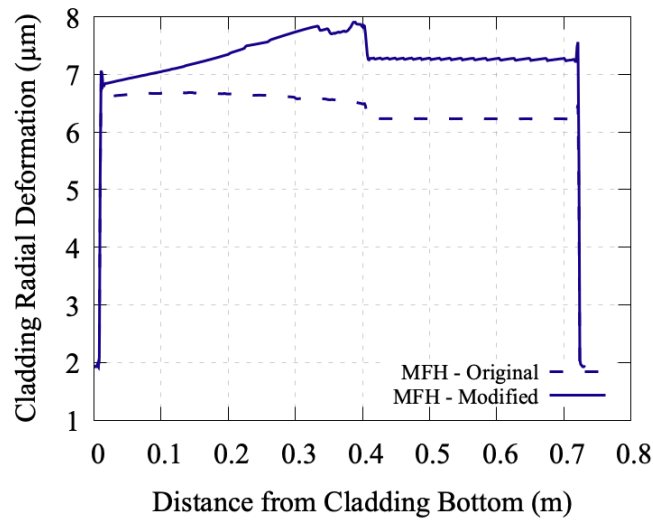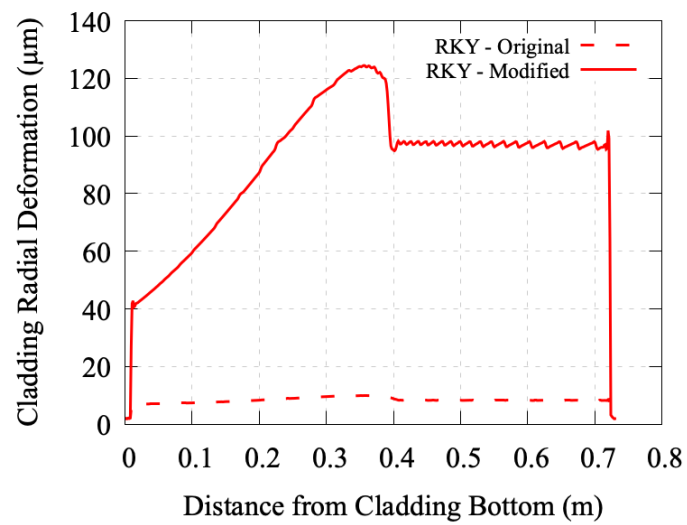
Figure 3.20. Difference in radial displacement along the cladding for a fuel pin from the X441 sub-assembly using the modified and original RKY creep model.

4. Summary and Conclusions

A mechanistic, physics-based creep model developed at LANL had been implemented into the BISON fuel performance code. This report documents simple testing of that model to evaluate its creep rate calculations in conditions relevant to the use of HT-9 as an advanced reactor cladding material. In a parallel effort, empirical HT-9 creep models in BISON have been modified to more appropriately calculate primary creep. These models have been used where applicable to calculate cladding strain profiles for an EBR-II fuel pin.

Features of the ROM have been discussed with the LANL development team, and refinements to the ROM are expected to be implemented into the HT-9 LAROMance model. After model improvements, this model will then be tested again under relevant conditions. Empirical models will also be updated to include the calculation for tertiary creep in the MFH model and strain recovery as cladding loading is dynamically adjusted or reversed. Further, these models are expected to be applied more broadly as more information from the Fuels Irradiation & Physics Database database is incorporated into BISON.

Bibliography

[1] DS Gelles. "Development of martensitic steels for high neutron damage applications". In: *Journal of nuclear materials* 239 (1996), pp. 99–106.

[2] JL Straalsund and DS Gelles. *Assessment of the performance potential of the martensitic alloy HT-9 for liquid-metal fast-breeder-reactor applications*. Tech. rep. Hanford Engineering Development Lab., Richland, WA (USA), 1983.

[3] R.G. Pahl, C.E. Lahm, and S.L. Hayes. "Performance of HT9 clad metallic fuel at high temperature". In: *Journal of Nuclear Materials* 204 (1993), pp. 141–147. ISSN: 0022-3115.

[4] Jacob A. Hirschhorn et al. "Metallic Fuel Performance Benchmarks for Versatile Test Reactor Applications". In: *Nuclear Science and Engineering* 0.0 (2022), pp. 1–25.

[5] Wei Wen et al. "Mechanism-based modeling of thermal and irradiation creep behavior: An application to ferritic/martensitic HT9 steel". In: *International Journal of Plasticity* 126 (Nov. 2019).

[6] Aaron E Tallman et al. "Surrogate modeling of viscoplasticity in steels: Application to thermal, irradiation creep and transient loading in HT-9 cladding". In: *JOM* 73.1 (2021), pp. 126–137.

[7] Lynn Brendon Munday et al. *Multiscale-informed modeling of high temperature component response with uncertainty quantification*. Tech. rep. Idaho National Lab.(INL), Idaho Falls, ID (United States); Los Alamos ..., 2020.

[8] Wei Wen et al. "Mechanism-based modeling of thermal and irradiation creep behavior: An application to ferritic/martensitic HT9 steel". In: *International Journal of Plasticity* 126 (2020), p. 102633.

[9] GL Hofman et al. *Metallic fuels handbook*. Tech. rep. Argonne National Lab.(ANL), Argonne, IL (United States), 2019.

[10] Ho Jin Ryu, Yeon Soo Kim, and A.M. Yacout. "Thermal creep modeling of HT9 steel for fast reactor applications". In: *Journal of Nuclear Materials* 409.3 (2011), pp. 207–213. ISSN: 0022-3115.

[11] Albert Casagranda et al. "Assessment approach to advanced fuel models". In: (Sept. 2021).